Publications of the Astronomical Society of the Pacific, 134:065001 (14pp), 2022 June https://doi.org/10.1088/1538-3873/ac71cc

Laboratory and On-sky Testing of an InGaAs Detector for Infrared Imaging

Kristoffor Batty[1], Iain Steele, and Chris Copperwheat
Astrophysics Research Institute, Liverpool John Moores University, Liverpool Science Park IC2, 146 Brownlow Hill, L3 5RF, UK; k.batty@2016.ljmu.ac.uk
Received 2022 February 14; accepted 2022 May 20; published 2022 June 22

Abstract

We describe the results of testing a shortwave infrared CMOS camera using an indium gallium arsenide (InGaAs) detector. The new generation of InGaAs detectors offers a cost-effective alternative to mercury cadmium telluride (HgCdTe) for astronomy research, with current, off-the-shelf cameras requiring no modification before use. Testing was conducted in the laboratory and on-sky while mounted to the robotic, 2 m Liverpool Telescope using a *H*-band filter. The camera exhibits a dark current of 821 e^{-} s^{-1} pix^{-1} and a bias level of 864 e^{-} pix^{-1}. The dark current associated shot noise is of similar size to the read noise of 32 e^{-} pix^{-1} in one-second exposures. Linearity within the count region where readout noise and bit-depth saturation effects are not dominant is within a few tenths of a per cent. After field-compression by fore optics, the plate-scale yields $0\farcs3$ pix^{-1}, near perfect for Nyquist sampling at the La Palma site. The sky background for the *H*-band filter dominates the other noise sources for the instrument for one-second exposures producing sky-limited photometry. On-sky observations show that milli-magnitude precision is achieved for sources <10.7 mag and a signal-to-noise ratio of 10 is achievable for 16th magnitude with a 3 minutes total exposure time, making it an ideal follow-up instrument for sources detected in current and upcoming IR surveys.

Unified Astronomy Thesaurus concepts: Infrared photometry (792); Astronomical instrumentation (799); Astronomical detectors (84)

1. Introduction

The sensitivity of modern, wide-field, optical transient surveys such as the Zwicky Transient Facility (ZTF) (Bellm 2014), Pan-STARRS (Magnier et al. 2020) and ATLAS (Tonry et al. 2018) has resulted in the discovery of a wealth of new objects and phenomena, making time-domain astrophysics a current and high-profile area. However, a comparative lack of survey capacity in Infrared (IR) has left the IR transient sky relatively unexplored. The ability of IR to image in dust-obscured environments enables investigations of objects and events unobtainable through optical surveys, and so there is a significant potential for discovery. The SPIRITS survey (Kasliwal et al. 2017) demonstrated this potential with the discovery of 14 previously unknown transients in nearby galaxies and has paved the way for more ambitious surveys to be commissioned (Lourie et al. 2020; Soon et al. 2020).

A class of transients of particular current interest is the electromagnetic (EM) counterpart to a compact binary merger (CBM)—an elusive transient involving a short gamma-ray burst (sGRB) and a Kilonova (KN). To date, this has only been observed with the accompanying gravitational wave signal once in the event of GW170817 (Abbott et al. 2017). IR follow-up will be a crucial component of counterpart identification searches. This reason is two-fold: First, the space density of binary neutron star (BNS) mergers is much lower than initially thought; thus, the rate of events paired with an on-axis sGRB is also low (Abbott et al. 2016). Second, photometric observations of GW170817 show a transient with a very rapid color evolution (Pian et al. 2017; Smartt et al. 2017; Tanvir et al. 2017), shifting the peak to the infrared on a timescale of days and decaying over the course of weeks. This rapid spectral evolution of the emission highlights the important role that an IR imager on a robotic telescope like the Liverpool Telescope (LT) (Steele et al. 2004; Copperwheat et al. 2016) can play in the characterization of future merger events.

The positional uncertainty of any event can be a hundred to tens of square degrees, meaning that the transient searches find large numbers of candidates due to unrelated sources. The role of telescopes such as the LT, with a field-of-view on the scale of arcminutes, is therefore in the follow-up of these candidates. Instruments capable of rapid IR photometry will therefore be a powerful tool in positively identifying the true counterpart among multiple possible candidates through their distinctive rapid color evolution and could make a decisive impact in upcoming LIGO-Virgo-KAGRA observational runs.

Infrared capability is relatively rare when compared to optical on smaller (~2 m class) telescopes. A prime reason for this is that traditional (InSb and HgCdTe) IR detectors rely on

[1] Author to whom any correspondence should be addressed.

exotic materials and fabrication techniques with a high per-pixel cost. These detectors often require additional cooling systems that can be difficult to maintain. The recent development of hybrid InGaAs/CMOS cameras with inbuilt air cooling systems offers a potential alternative with lower cost and high performance.

The use of InGaAs detectors as a cost-effective replacement for HgCdTe in astronomy is an idea that has gained traction over recent years. An initial study using a customized InGaAs detector found that by reducing read noise through non-destructive readout, InGaAs detectors could be competitive to HgCdTe in applications that do not require *K*-band imaging (Simcoe et al. 2019). Further study showed the effectiveness of InGaAs detectors to study bright sources with large pixel well depth or NIR sky surveys, provided the pixel size was large enough to achieve sky-limited results (Strausbaugh et al. 2018). Our study continues this theme by using an off-the-shelf camera mounted onto the 2 m Liverpool Telescope with only a fore optics modification to compress the field and achieve Nyquist sampling.

This paper aims to assess the capabilities of a commercial InGaAs camera system for astronomical imaging in the short wavelength infrared (SWIR). For the instrument to succeed in its scientific goal as a follow-up instrument, it must achieve sky-limited photometry in the *H*-band with an ideal pixel scale for Nyquist sampling at the La Palma site. In Section 2 we introduce the instrument design and provide a theoretical model for sensitivity. Section 3 will provide the laboratory characterization, while Section 4 will focus on on-sky results.

2. Instrument Design

2.1. Detector

The detector has a sensor format of 640×512, $15\ \mu\text{m} \times 15\ \mu\text{m}$ active pixels and was manufactured by Semi Conductor Devices USA (SCD-USA). It is integrated into an off the shelf camera system by Raptor Photonics (UK) as their Ninox-640[2] product, which incorporates an air-cooled thermo-electric cooling system capable of cooling to ∼40°C below ambient. All data produced for this paper, unless otherwise specified, is taken with a recorded sensor temperature of −20°C, which is the normal operating temperature for this model. This temperature was found to be held to better than 1°C in all of our testing.

The detector uses a thinned Indium Arsenide and Gallium Arsenide (InGaAs) alloy and has an effective bandwidth of 550–1700 nm. Incident photons are converted to electrons in the InGaAs focal plane array (FPA) and transferred to a CMOS readout integrated circuit (ROIC) via indium dots to read the image. The capacitive transimpedance amplifier (CTIA) circuit structure for the ROIC boasts excellent linearity, sensitivity and low-noise performance (Hsieh et al. 1997). A benefit of CMOS is that, unlike CCDs, no charge transfer is needed between pixels. Instead each pixel is addressable through an array of column and row selection switches that can connect it to a dual 8/13-bit analog-to-digital converter in a glueless video graphics array. This allows reconstruction to a traditional 14-bit readout, with 16 channels of readout possible in parallel. Manufacturing of the array results in a thin substrate of Indium Phosphide (InP) encasing the InGaAs layer which begins to absorb photons with wavelengths below 900 nm. The camera can be read out in one of two gain modes; High gain offers a low pixel well-depth (∼10,000 e^-) and low readout noise (∼37 e^-), and Low gain, which offers high well-depth (∼650,000 e^-) with high read noise (∼163 e^-). This high read noise would limit our ability to image faint targets and therefore, high gain was chosen for all of our testing.

The InGaAs bandgap of 0.75 eV causes a sharp drop off at wavelengths above 1700 nm. Figure 1 shows the published quantum efficiency (QE) curve supplied by Raptor Photonics Ltd. The SWIR region is the best performing with a QE of ∼80% showing good results can be expected using *Y*, *J* and *H*-band.

Readout of the detector was accomplished using a Camera-Link interface board housed within a small format PC running the Linux operating system. The supplied software application programming interface (API) was used to develop a simple Linux application allowing data acquisition and writing of FITS format data files. The total time overhead for each image is the requested exposure time with an additional 1.5 s for exposure resets and writing to disk. For the purpose of this work all "in camera" image correction (bad pixel masking, nonlinearity and automated dark correction) was disabled.

2.2. Optical Design

The instrument is intended for use on the Liverpool Telescope (Steele et al. 2004), which is a Ritchey–Chrétien telescope with a 2 m primary mirror and a focal ratio of $f/10$ at the Cassegrain focus. This yields a plate scale of 97 μm arcsec^{-1} in direct imaging. In this mode of operation, each 15 μm pixel of the instrument would subtend 0.″15, which would be likely to oversample the typical site seeing and give a rather small field of view. We therefore designed a simple field compressing foreoptic to quicken the focal ratio for the instrument to ∼$f/5$. This allows for a field of view of $3.'3 \times 2.'7$ with a pixel scale of 0.″3. This theoretical value is near-perfect for Nyquist sampling with the average optical seeing at the telescope site (the Observatorio del Roque de los Muchachos on the Canary island of La Palma) being ∼0.″7 FWHM (corresponding to 1.″3 80% encircled energy).

The optical design (Figure 2) uses a 200 mm focal length achromatic doublet (Thorlabs AC508-200-C) situated 135 mm

[2] Technical information at: https://www.raptorphotonics.com/wp-content/uploads/2015/10/Ninox_UM_REV1.pdf.

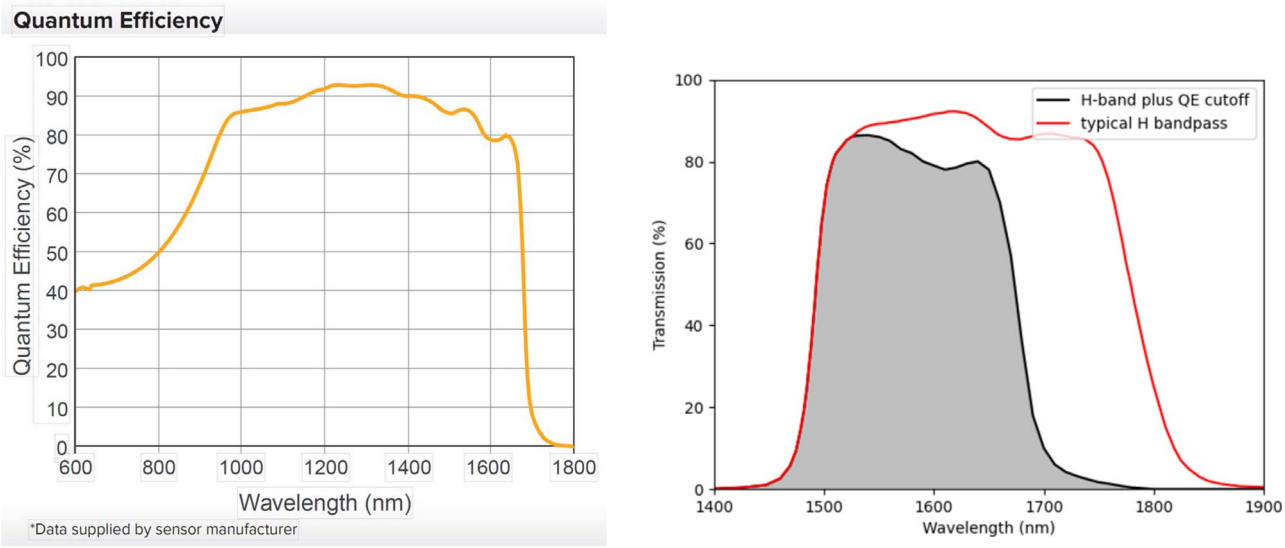

Figure 1. Left, quantum efficiency curve published by Raptor Photonics for the InGaAs detector model used taken at the operating temperature of −20°C. The curve shows >80% efficiency for ∼1000–1600 nm Image courtesy of Raptor Photonics Ltd. Right, a comparison of transmission data for a typical *H* bandpass and our *H*-band plus long band cut-off.

in front of the telescope focal plane as a field compressor. This provides most of the focal ratio change and is followed by a 200 mm focal length BK7 plano-convex lens (Thorlabs LA1256-C) which corrects the resulting focal plane to a flat surface. Both lenses are standard catalog items and are equipped with SWIR optimized anti-reflection coatings (providing <0.5% reflectivity between 1050 and 1700 nm). It should be noted that the optical design does not incorporate a reimaging pupil, meaning that a cold-stop could not be implemented to block excess thermal emission from the telescope structure. This limits the applicability of the optical design to *H*-band and shorter wavelengths.

The field compressor is followed by a 1500 nm longpass filter (Thorlabs FELH1500) which in combination with the long wavelength cutoff of the detector yields a response reasonably close to the standard astronomical *H*-band. Figure 1 (right) compares our effective *H* filter response to a standard astronomical *H*-band from another LT instrument. This plot shows a significant drop in efficiency for longer wavelengths. The instrument would benefit from color correction with accompanying *J*-band images in future photometry, however, this paper will focus solely on the results obtained in our pseudo-*H*-band.

The combined prescription of the telescope and instrument is presented in Table 1. Ray tracing of the design gives a monochromatic 80% encircled energy value of $<0\farcs2$ diameter at the field center and $<0\farcs3$ at the field edge. Chromatic aberration over the wavelength range 1500–1700 nm contributes $<0\farcs1$ of additional image degradation. Overall the optical design is predicted to have little effect on delivered image quality which will be dominated by atmospheric seeing.

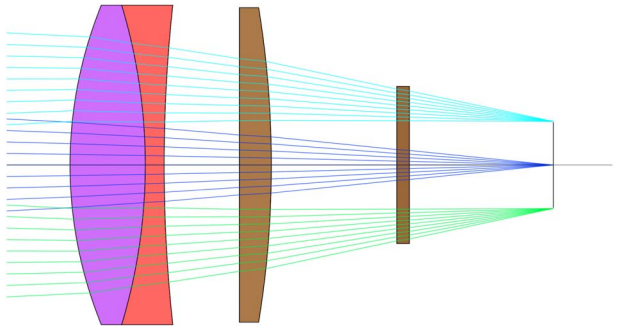

Figure 2. Field compressor optical design. From right to left are the field compressing achromat, a field flattening plano-convex lens and the filter.

2.3. Mechanical Design

The optical design was implemented using commercial off-the-shelf lens tubes incorporating all optical elements (lenses and filters) and terminated by a C-mount thread that could be directly attached to the camera. The total weight of the lens and camera combined was ∼1 kg. For mounting to the telescope the camera body was attached to a a standard LT instrument mounting plate. This allows the instrument to be fed by the beam folding mirror within the telescope Acquisition and Guidance box.

2.4. Predicted Sensitivity

In Figure 3 we show the theoretical sensitivity as a function of limiting magnitude with respect to total exposure, plotting lines of constant signal-to-noise. Read noise and dark current values were taken from early testing of bias and dark frames

Table 1
ZEMAX Format Optical Prescription

Number	Comment	Type	Radius	Thickness	Glass	Semidiameter
0		Standard	inf	inf		1000.0000
1	M1	Asphere	−12000.0000	0.0000	MIRROR	1000.0000
2		Standard	inf	−4315.3850		1000.0000
3	M2	Asphere	−4813.0000	0.0000	MIRROR	308.0000
4		Standard	inf	5480.0000		308.0000
5	AC508-200-C	Standard	67.1400	12.0000	N-LAK22	25.4000
6		Standard	−87.5700	3.0000	N-SF6HT	25.4000
7		Standard	234.2700	12.0000		25.4000
8	LA1256-C	Standard	inf	5.1000	N-BK7	25.0000
9		Standard	−154.5000	20.0000		25.0000
10	FILTER	Standard	inf	2.0000	F_SILICA	12.5000
11		Standard	inf	22.9666		12.5000
12	DETECTOR	Standard	inf	0.0000		6.8000

Note. All dimensions in mm. The conic constants of the telescope primary and secondary mirrors are −1.0703 and −4.179 respectively.

with values of 32 e^- and 1579 ADU per second respectively. We estimated system throughput reduced by ∼50% compared with the theoretical value due to the inaccessibility of the site for the maintenance team to clean the telescope mirrors during pandemic restrictions. This gives a Vega system zero-point of 22.9 mag for the *H*-band filter, expected to rise by ∼0.5 mag once maintenance recommences. The sky brightness in the *H*-band has been taken to be 13.5 mag (Benn & Ellison 1998), and an aperture size of 1.2× the average seeing at the La Palma site was used. This figure shows that an SNR of 10 should be achievable at an exposure time of 150 s for point sources of $H = 16$. This is well-matched to the discovery capabilities of modern IR surveys such as Palomar Grattini, which has the same limiting magnitude (Moore et al. 2016).

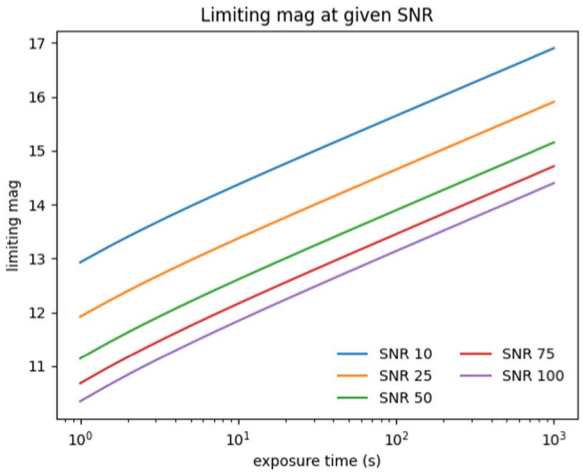

Figure 3. Theoretical limiting magnitude as a function of exposure time for a set signal to noise ratios once mounted on to the Liverpool Telescope. The curve has been calculated from manual and telescope specifications and will be compared to on-sky data in Section 4.1.

3. Laboratory Characterization

3.1. Experimental Setup

Laboratory testing was conducted in a low dust (clean room) environment using a tungsten light source to illuminate a flat-screen. The luminosity was controlled by varying the input power to the light source. To obtain accurate dark frames we positioned a gold plated mirror in front of the lens to ensure the detector was viewing its own cold reflection rather than a room temperature scene. To further reduce the risk of any light leak, tests were conducted in the laboratory dark room.

Since zero-second exposures are not possible with CMOS architecture cameras, bias frames were estimated through extrapolating a series of dark frames of different exposure times back to zero seconds for each pixel. These were compared to minimum exposure (100 μs) frames which showed a mean excess of ∼200 ADU. This spurious generation of electrons during minimum length exposures would skew bias results and therefore the extrapolated method was preferred.

3.2. Linearity

Fundamental to the operation of imaging sensors is the conversion of photonic input to electronic output. This transfer should happen linearly with the amount of light incident on the detector. Historically, current-mode CMOS detectors have had nonlinearity levels unacceptably high for wide-scale use, unlike CCDs which can normally achieve nonlinearity of a few tenths of a percent. Advancements in readout integrated circuits have gone a long way in combating this issue and modern CMOS cameras have reported excellent nonlinearity results (Wang & Theuwissen 2017).

Analysis of nonlinearity across the array can be seen in Figure 4. The data were obtained through varying exposure times under uniform illumination. The median values of counts through the time series was used to model a predicted linear

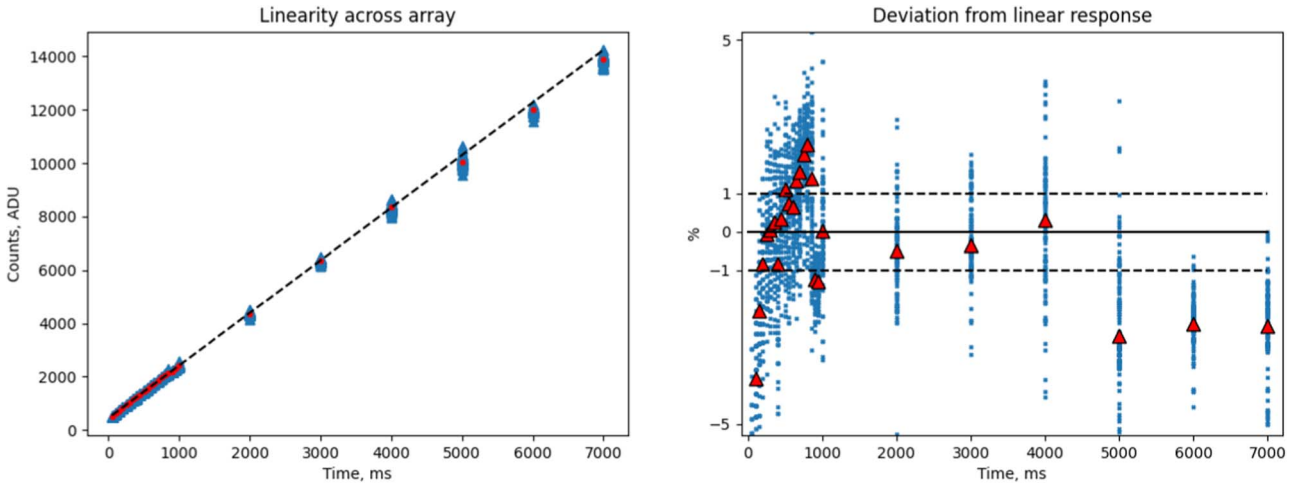

Figure 4. Linearity results for statistics across the array. Data were gathered from 200 images under constant light while varying exposure times. Left shows counts vs. exposure time used to model linear behavior. Right is a comparison of data points against the model by taking the ratio of the measured values against those expected from linear response to exposure time.

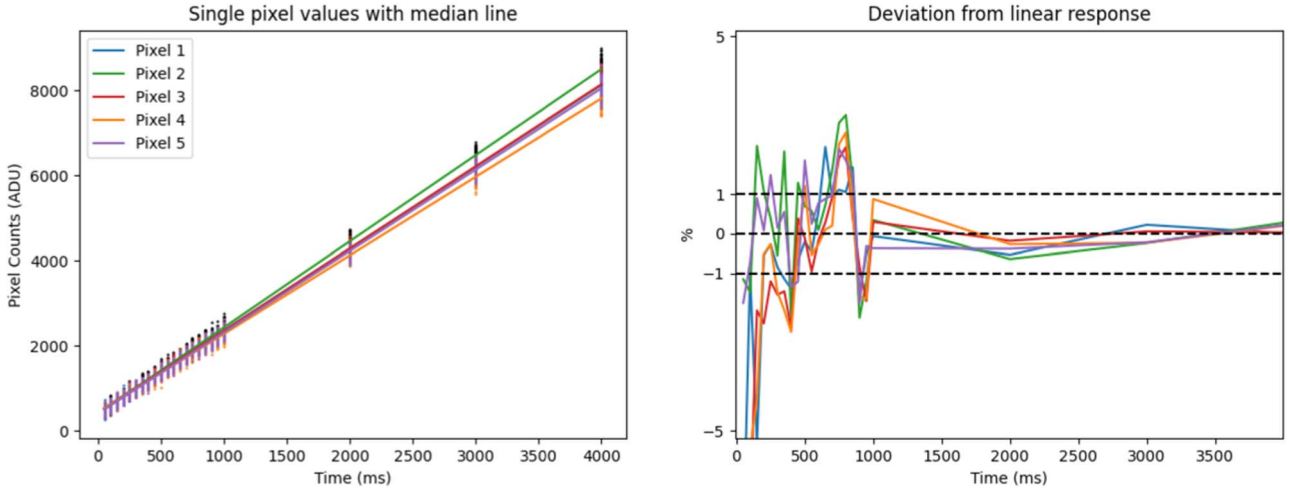

Figure 5. Linearity tests for 5 randomized pixels in the array. Data were produced with the same methods used in Figure 4 but on an individual pixel basis.

behavior in which individual frames could be compared to determine nonlinearity percentages. We see a large spread in values at low counts due to the dominance of read noise. This behavior is no longer followed once we reach a count level of ∼3000 ADU as at this point, the shot noise surpasses it and we see a linear behavior of within 1% through the rest of the series up until 5 s. Above 5 s, pixels begin to approach the ADC bit-depth (rather than pixel well depth) saturation levels. Increasing light levels no longer produces a linear response and therefore, the linearity across the array is skewed. Exposure times of 5 s or greater were therefore removed from subsequent tests.

The architecture of CMOS cameras is such that each pixel has its own inverting amplifier and integrating capacitor. It is therefore important to study not just how the array behaves as a whole to increased light levels, but individual pixels as well. The results of tracking 5 pixels through the times series are shown in Figure 5. Expected values were calculated for each pixel using the linear relationships displayed in the counts versus exposure time graph. Similar to the results of Figure 4, measurements of low count levels shows the dominance of readout noise resulting in a large variation when compared to the expected values. Consistent with previous results, once a counts of 3000 ADU is surpassed, nonlinearity is within 1% for each pixel measured up until bit-depth saturation levels.

3.3. Dark Current

To study the dark current of the instrument, dark frames were acquired for intervals of system temperature and

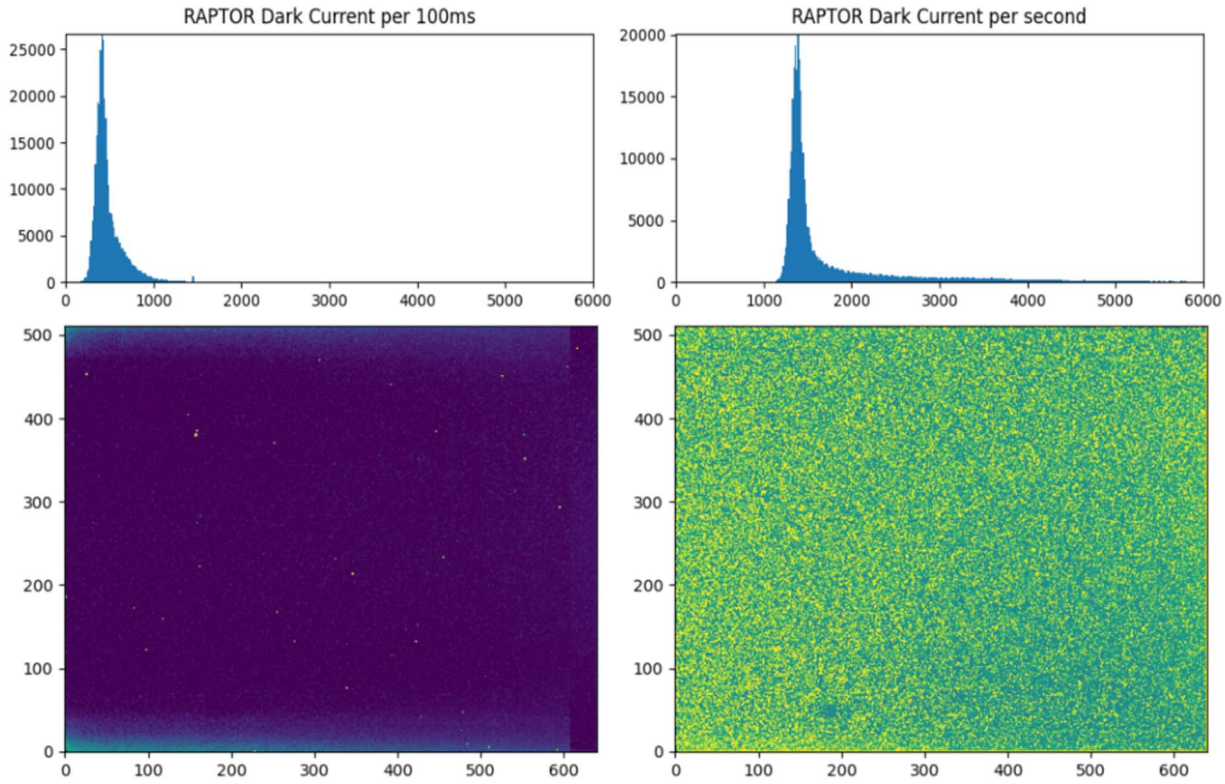

Figure 6. Histogram plot of measured pixel values across a median stack of 200 images (top) displayed with the stacked dark frame from the data (bottom). This was done for 100 ms (left) and 1000 ms (right). The camera was operated at −20°C which is the normal operating temperature for the instrument. The darks have been bias subtracted.

exposures. The dark frames can be extrapolated backwards to 0 s and reconstructed to a bias frame for subtraction to reveal true dark current per Section The extrapolated bias frame has a median count of 1662 ADU and displays significant edge glow along the top and the bottom of the image (Figure 10). This glow can be attributed to an increased dark current due to the absence of the thermal electric cooling (TEC) in these regions. The results of varying exposures are shown in Figure 6. The histogram values show the expected normal distribution with a long tail present in 1000 ms due to the presence of a large number of warm pixels in the array (see Section 3.5). This tail significantly skews the mean value to 1579 counts, with the peak of the distribution at 1142.

Figure 7 shows a power-law proportionality in dark signal and temperature. The small bandgap of the InGaAs alloy means that it is easy to thermally generate electrons resulting in a significant dependence of the dark signal on temperature. Results of the individual pixels show some behavior of the fixed pattern noise (FPN) in the system. First is the tendency toward warm pixels over cool, and second, the deviation in the scatter from median counts increases with temperature of the sensor. Therefore, it is vital to cool the system to reduce this dark signal and the amplitude of its noise. the instrument is

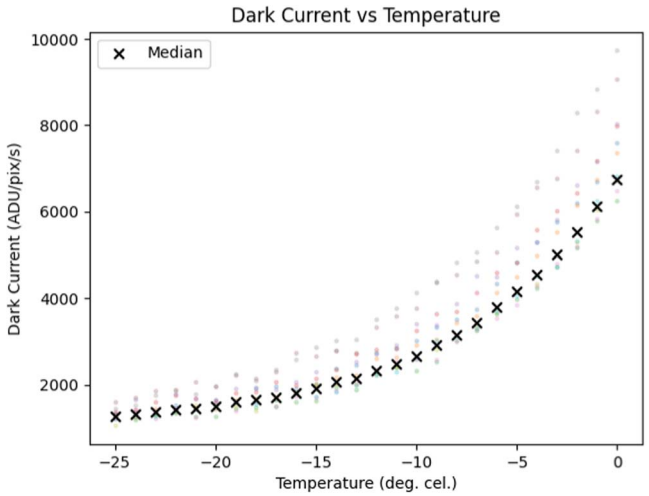

Figure 7. Results of dark current values with respect to temperature for the instrument. The median value across the frame has plotted in black, whereas the transparent data points are individual pixels chosen at random across the array.

stable with its onboard cooling system to remain stored and operated at −20°C. This corresponds to a dark signal of 1579 ADU $\mathrm{pix}^{-1}\,\mathrm{s}^{-1}$ and dark shot noise of ∼55 ADU $\mathrm{pix}^{-1}\,\mathrm{s}^{-1}$ which is of similar size to the read noise.

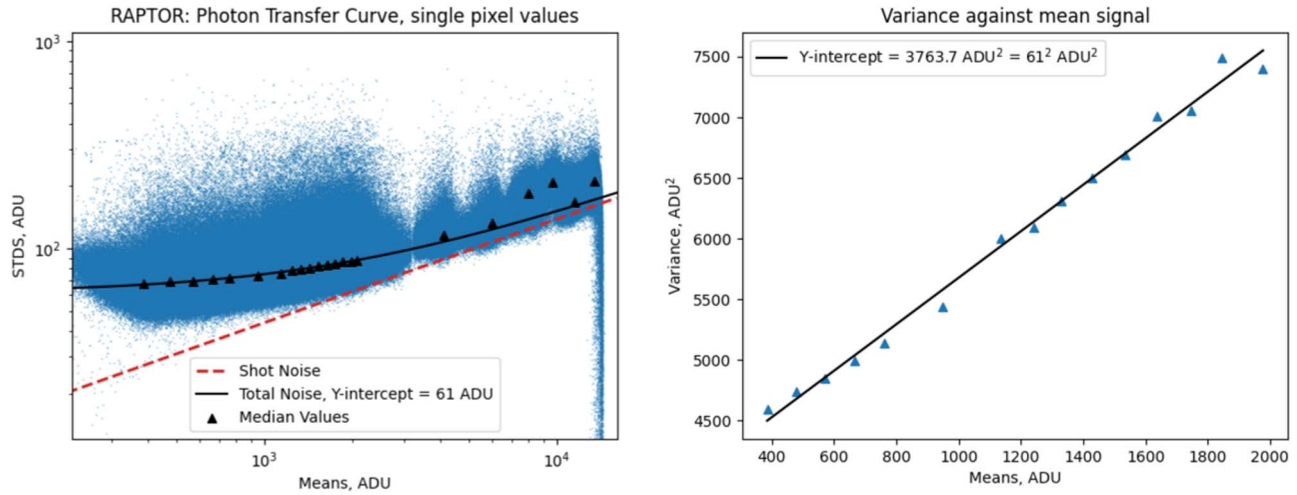

Figure 8. Photon transfer curves for the instrument. These were created through a series of 200 images under uniform illumination with varying exposure times. Left, we show the standard deviation for individual pixels on a log–log scale with data points (blue) and median values for each interval (black triangles). The shot noise has been modeled using the gain of the system and is included as a red dashed line. On the right is the median variance of the central 100 × 100 pixels against measured counts.

3.4. Photon Transfer Curve

The photon transfer curve (PTC) is the dependence of noise against the measured signal and is shown in Figure 8 as a measure of variance against the signal, on a linear axis, and standard deviation (STD) against the signal, both on a log–log scale. It allows users to quantify the camera's performance and verify the sensor's gain.

The PTC is often constructed by studying noise across frames under uniform illumination. The issue for this method on CMOS detectors is that the increased FPN in the system (see Section 3.6) causes a large noise distribution across pixels. We therefore chose to track individual pixels through a series of images. For each time interval, a series of 200 images were taken and pixels within a 100 pixel border were tracked and measured with the results shown in Figure 8.

In the standard deviation image, individual data points (blue) show a large noise distribution from pixel to pixel as expected with the high FPN. For clarity, median values for each interval have been super-imposed as black triangles. The total noise of the system is the sum of its parts, which in this case, is the read noise along with dark and signal shot noise.

We see a good agreement between median values and the total noise line present in the system. There is an increased deviation from this line as we approach bit-depth saturation as shown by the rapid drop off in noise at a signal of 14k ADU. It is theoretically possible to determine the conversion gain from this standard deviation plot provided we reach a region dominated by shot noise. This behaves as Poisson and would therefore have a gradient of 0.5 shown by the red dashed line. However, due to a high read noise of $\sim$32 e^-, this is only achieved for a small region close to bit-depth. Instead, the gain can be measured by inverting the gradient between the variance of pixels against the measured signal. The variance plot was produced by tracking the central 100 × 100 pixels through the series of 200 images at each time interval. The median value for pixel variance at each increment was taken to produce a singular point on the PTC. Doing this with the data in Figure 8 gives a result for the gain of 0.52 e^- ADU^{-1}. The *y*-intercept in both graphs can be used to check read noise which is consistent between the two figures. We note that this conversion gain is rather over-sensitive for an array with a read noise of 32 e^- where Nyquist sampling theory would suggest a gain $\sim$16 e^- ADU^{-1} would be more appropriate and allow longer integrations before approaching bit-depth saturation. However the alternative low gain option provided by the camera manufacturer unfortunately has very high read noise of $\sim$163 e^- and is therefore not usable in our application.

3.5. Pixel Noise

To study individual pixel noise, a single-pixel was tracked through a series of 2000 images. The shot noise of this pixel will follow a normal distribution in which 99.7% of points are within 3σ of the mean. Our results show many outliers that we attribute to random telegraph signal (RTS). The RTS is generated in the electronics as the capture and release of charge at defect sites which causes a discrete switching in device resistance. As such, it results in sudden transitions between readings at unpredictable times (Leyris et al. 2006). Figure 9 shows the results of this test. All images display classic random telegraph signal (RTS) properties, with the 100 ms images showing a far more severe response than the 1000 ms images. At 1000 ms, the Poisson noise is close to exceeding

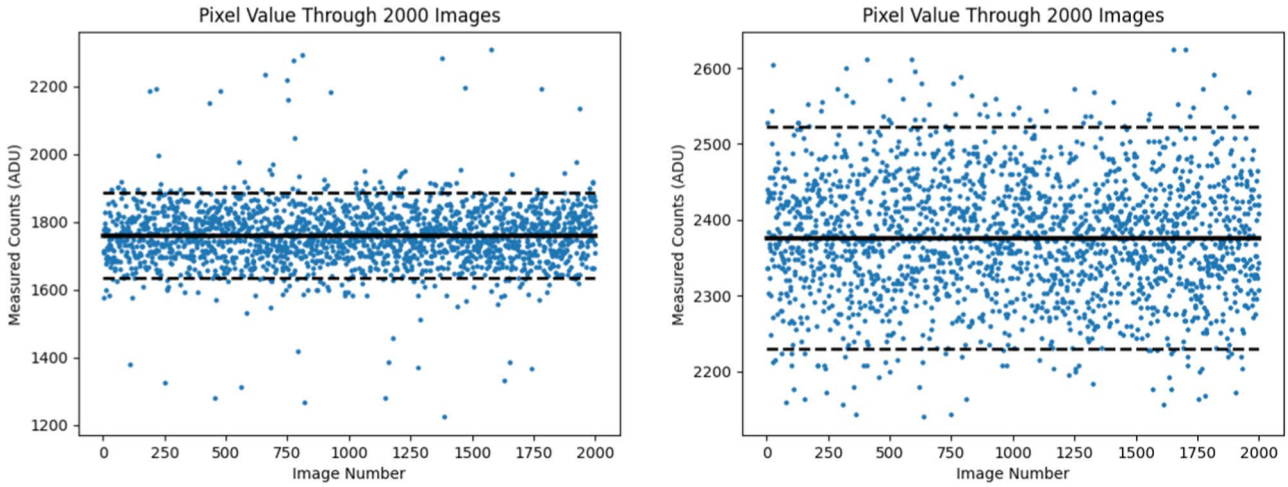

Figure 9. A single-pixel chosen at random has been tracked through a series of 2000 100 ms (left) and 1000 ms (right) images to test for individual pixel variation. All images have a superimposed dashed line representing a 3σ border and a solid line representing the median value.

Table 2
Results of Searching For Defective Pixels

Pixel Defect	Number of Pixels	Percentage of Total
Cool	11	0.003%
Cold	6	0.002%
Warm	74922	23%
Hot	86	0.03%
Above *H*-band sky counts s^{-1}	16906	5.16%

Note. Cool and warm pixels deviate from the mean count by over 3sv. Cold pixels are either non-operating pixels or pixels that only read bias levels and hot are pixels that are always saturated.

the RTS switches' amplitude; therefore, it does not have a strong influence on results. Images with other noise, such as sky background, should exceed this amplitude, therefore reducing the problem. This can also be removed by coadding frames or in extreme cases, sigma-clip stacking.

The production of the sensor has resulted in a subset of defective pixels across the instrument's array. These pixels can either be cold, cool, warm or hot. Cool and warm pixels are defined by being at least 3σ away from the mean count value while cold pixels are either showing 0 or bias level counts, and hot pixels are always saturated. A series of flat images were taken, and individual pixels were measured against the statistics across the sensor to find defects. The results of the investigation are displayed in Table 2 and show the expected tendency toward warm/hot pixels. Warm pixels are the most common feature due to the high dark current and FPN; however, image subtraction can easily mitigate this. The results show that the camera achieves a photosensitive pixel percentage of $>99.5\%$ advertised by Raptor Photonics. As we will not be using any in-camera image correction, including bad pixel masking, the effect of bad pixels when making observations will be removed through a dithering procedure, ensuring defective pixels are not imaging the same location twice within a series. For pixels to be operable for sky-limited, *H*-band imaging on the LT, the total detector noise must be below the sky count per second during observations. On-sky observations (see Section 4) show a mean sky brightness of 3900 ADU s^{-1}. Using this as a limit, we find that $\sim$94.8% of pixels have noise levels below sky-background and are therefore considered operable.

3.6. FPN

FPN is the spatial variation across an image of uniform illumination due to some device parameters that appears as a recurring pattern of cool and warm pixels. It is a general term often including dark signal and photoresponse non-uniformity across the array, which both react linearly with counts. CMOS detectors typically have higher FPN than their CCD counterparts and can suffer from both pixel FPN, caused through individual pixel transistors, and column FPN, caused by column amplifiers for readout. The FPN for the instrument can be seen clearly in the bias image of Figure 10. Here we can see several features including pixel and column noise features, photoresponse non-uniformity resulting in a gradient across the image, and a severe edge glow across the top and the bottom of the array. This edge is caused by an increase in dark current in these regions due to the absence of the TEC system for the edges of the detector (see Section 3.3). This problem persists in dark subtracted flats in which this region shows a low photoresponse to an illuminated source. The dark signal non-uniformity can be removed via image subtraction, whereas the low photoresponse across the edges of the image can be corrected using flat fields.

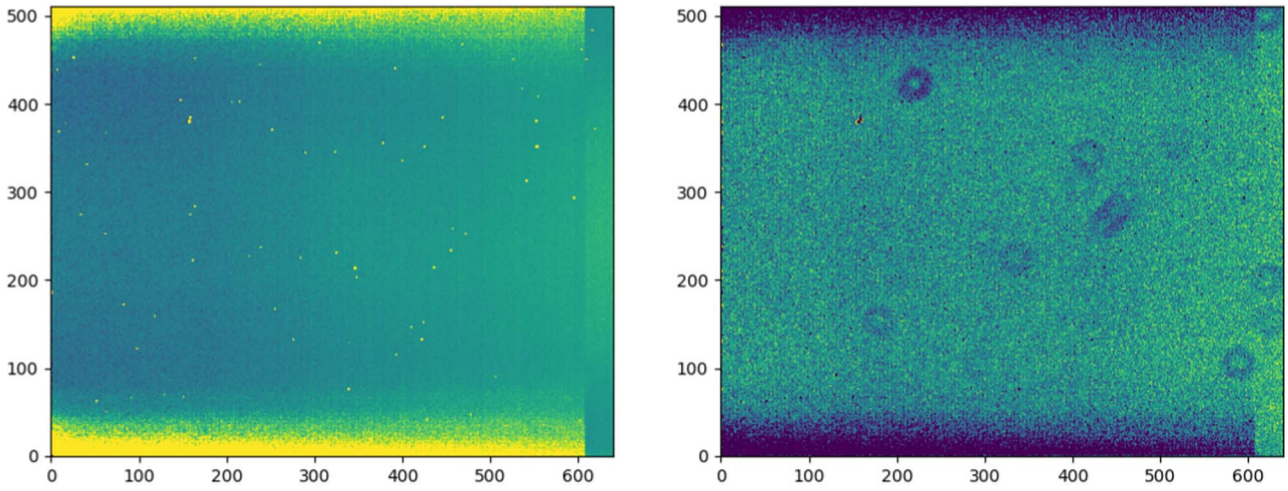

Figure 10. Extrapolated bias (left) and flat frame (right) for the instrument. The edge glow present in the bias frame corresponds to a photoresponse non-uniformity for the flat field image with a sharp cutoff at $x = 608$ pixels.

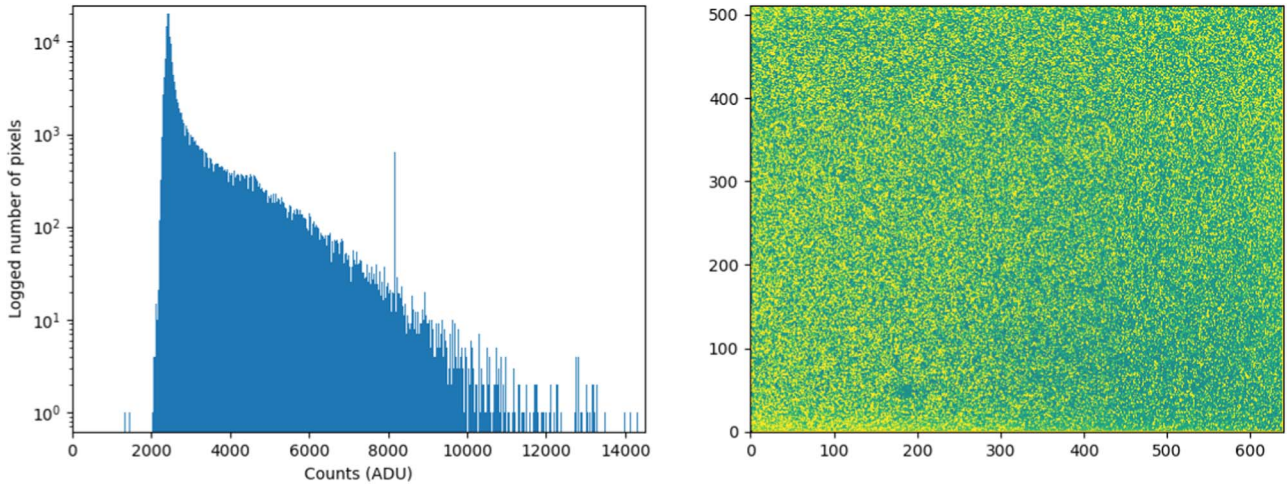

Figure 11. Log-scale histogram (left) of the stacked dark frame (right) showing remaining rms after reducing Poisson noise present to a factor of 1.

Further analysis of the FPN is shown in Figure 11. The frame used has a mean count of 1560 e^- which gives a shot noise of $\sim 40\,e^-$. By taking a median stack of 1600 images, we have reduced this shot noise by a factor of $\frac{1}{40}$. Therefore, the shape of the resulting histogram is dominated by the remaining FPN and read noise. By subtracting a fixed value for the read noise from the rms for this histogram, we estimate the FPN impact for this signal level to be 33% of the measured signal.

4. On Sky Testing

The instrument was mounted on the LT from 2021 January to August for on-sky testing. A list of objects and tests that were performed is given in Table 3. The first tests were image quality and the focus of objects at the center and the edge of the field. The FWHM was tested against secondary mirror position for multiple observations where the minimum radial FWHM was taken as the sharpest image (see Figure 12). Once point source focus was accurate, images were compared to catalogs to test the delivered plate scale against the fore optics design (see Figure 13). Results give an FoV of $3\farcm23 \times 2\farcm58$ which corresponds to a focal ratio of $f/5.11$.

Attention was then shifted to the camera capabilities and observational technique. As described in Section 2, there is a considerable amount of noise in the camera which must be addressed for accurate measurements. The most prominent noise features in the instrument are the dark signal and photoresponse non-uniformities. These can be removed through image subtraction and flat correction, provided

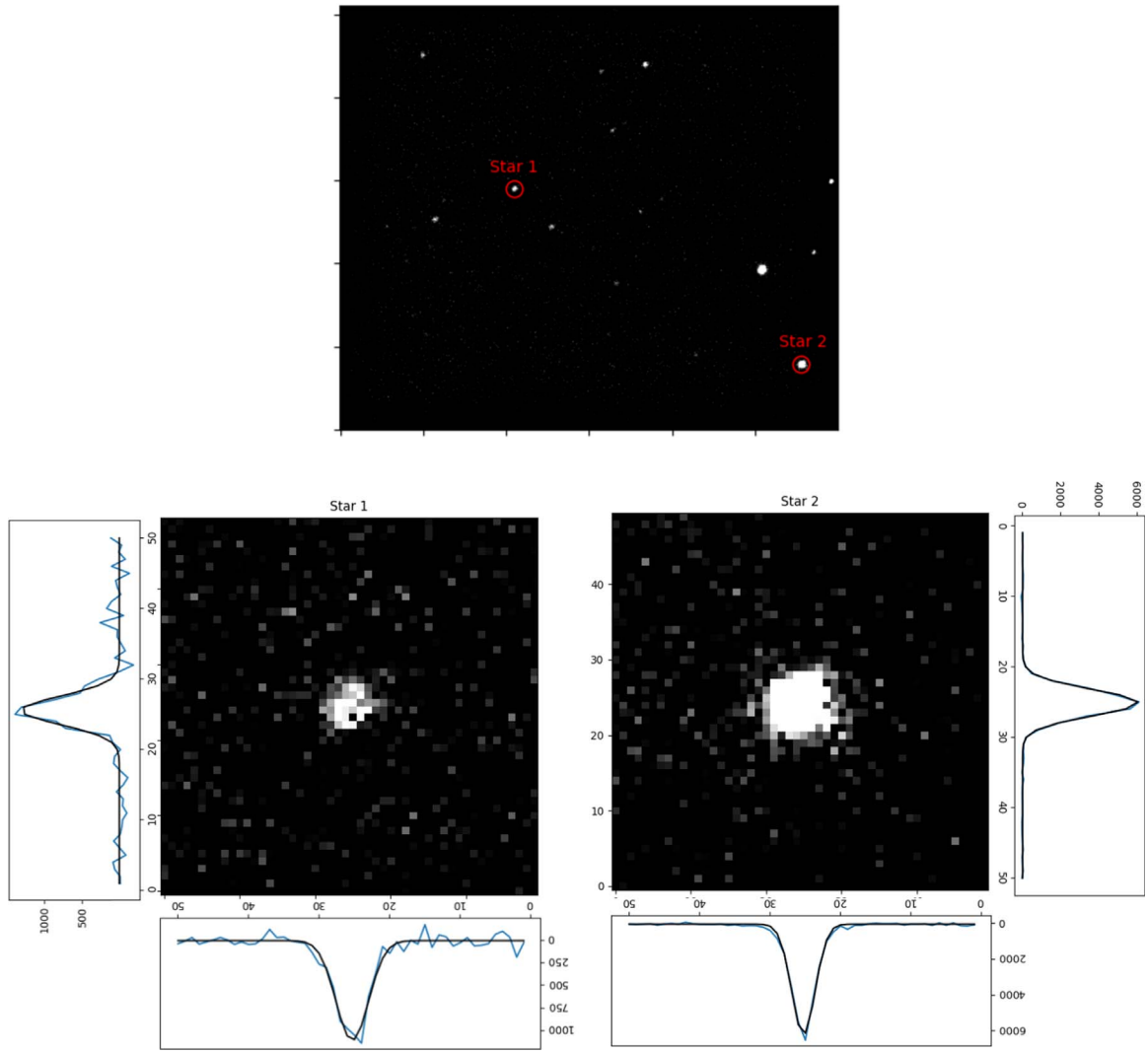

Figure 12. Images showing the process of focusing the instrument. Stars were chosen near the center and edge of field with the PSF measured until a minimum FWHM was achieved.

Table 3
Table Displaying Some On-sky Work Performed with the Instrument

Date	Target	Type	Magnitude	Result/Comment	ZP	Seeing at Zenith
26/01/21	36 Per	Star	4.44	Focus test	22.9	0.″64
	BD +23	Star	5.49	Focus test		
	HD 22781	Star	6.69	Plate Scale test		
	M 74	Galaxy	7.04	Dither Test		
19/02/21	TYC 3280-4-1	Star	10.27	Focus test	22.5	0.″57
	HD 50188	Star	9.47	Dither test		
	Wolf 134	Low-mass star	11.01	Standard star		
	GD 71	White Dwarf	13.90	Plate scale		
06/05/21	NGC 2506	Open cluster	⋯	Image quality	23	0.″52
	NGC 2420	Open cluster	⋯	Consistency test		
	M 3	Globular cluster	⋯	Dither test		
	NGC 4030	Galaxy	7.60	Data-reduction test		
18/05/21	NGC 2420	Open cluster	⋯	Consistency test	22.8	0.″52
	IC 3340	SNe	⋯	ATel #14636		

Note. Magnitudes displayed are cataloged *H*-band magnitudes as found by the 2MASS All Sky Survey (Skrutskie et al. 2006).

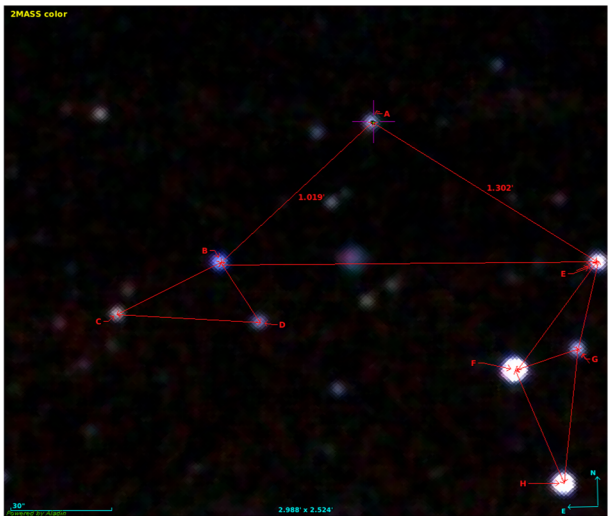

Figure 13. Cataloged 2MASS image of GD71 showing angular distances which were used to test delivered FoV of the instrument's field compressor.

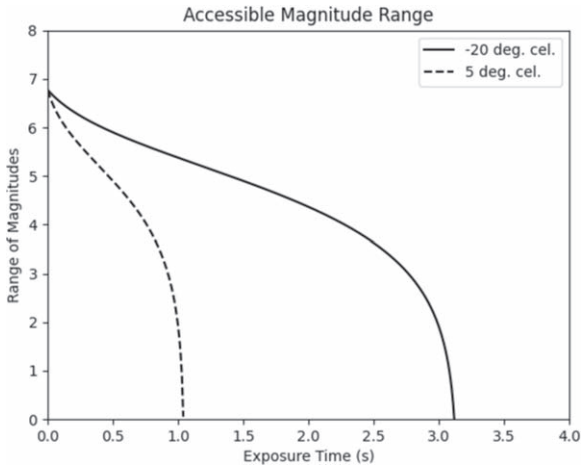

Figure 14. Theoretical accessible magnitude range based on an average sky count of ∼3900 ADU s^{-1} as found during observations. Dark current was taken as 1579 ADU s^{-1} for −20°C and 13,304 ADU s^{-1} for 5°C.

accurate dark and flat field frames can be obtained. Several methods to achieve the best dark frames were trialled. The highest signal-to-noise was obtained in the laboratory setting with a gold plated mirror positioned in front of the lens. Dark frames acquired using this method will be used with uniformly illuminated images obtained during twilight to create the flat field frame.

A significant noise source during data acquisition is the very bright IR sky background (on average ∼3900 ADU pix^{-1} s^{-1}). To address this, observations employ a 9-stage dithering technique during data acquisition. The dither consisted of 9″ or 1′ changes in position on and around the target by offsetting the telescope position. Calibration frames were then created through median stacking unaligned images, removing stars from the field, resulting in sky background and camera noise images. These were then subtracted from science frames during data reduction.

Using the dark current per second (DC), read noise (Er) and the average sky count rate (SR) we have calculated a theoretical accessible magnitude range (AMR) by:

$$\mathrm{AMR} = 2.5 \log\left(\frac{\mathrm{BDC} - B - (\mathrm{DC} \times t) - (\mathrm{SR} \times t)}{\sqrt{Er^2 + (\mathrm{DC} \times t) + (\mathrm{SR} \times t)}}\right). \quad (1)$$

Where BDC is the bit-depth capacity, B is the bias level, and t is the time in seconds. This was done for two temperatures to demonstrate the useful time range in which the camera can produce a specific dynamic range as shown in Figure 14. The sky background is the dominant source of counts and causes the dynamic range to drop rapidly with bit-depth saturation occurring at ∼3 s. The instrument's images are therefore composed of co-adds of shorter exposures to reach extended exposure times. These co-adds are combined through a mean stack to produce the data for a single dither position. This mean stack reduces the shot noise across the frame by a factor of $\frac{1}{\sqrt{n}}$ where n is the number of images in the stack and is therefore equivalent in signal to noise ratio to a single exposure of the same total length. The individual dither positions were then aligned and stacked using a median to remove any artefacts from the final image.

4.1. Photometric Results

NGC 2420 was chosen for testing as the open cluster had an even distribution of stars across the entire array. Camera consistency was tested through observations on 2021 May 6 and 2021 June 18 with results shown in Figure 15. Both images were taken using 20 co-adds of 1 s exposures in a 9 dither pattern for a total exposure time of 180 s. The dither overhead was ∼10 s per pointing, giving a total execution time including the 1.5 s per exposure readout overheads of 540 s, corresponding to an total observing time overhead of 200%. Matching stars across the frames and plotting the instrumental magnitudes of each date resulted in a tight correlation around a gradient of 1.0 demonstrating good consistency over that time period.

The instrument's sensitivity was investigated once observational and data reduction techniques had demonstrated consistent results and stabilized noise. Using images of NGC 2420, the SNR was measured for each star in the frame and plotted against the instrumental magnitude (see Figure 16). A theoretical line of sensitivity was calculated in the same manner as Figure 3 with updated values for the night's sky brightness and zero-point. The real data values for a total exposure time of 180 s are consistent with the theoretical expectation with a slight deviation on very bright sources as counts approach bit-depth levels. This also shows that co-adding 1 s images to

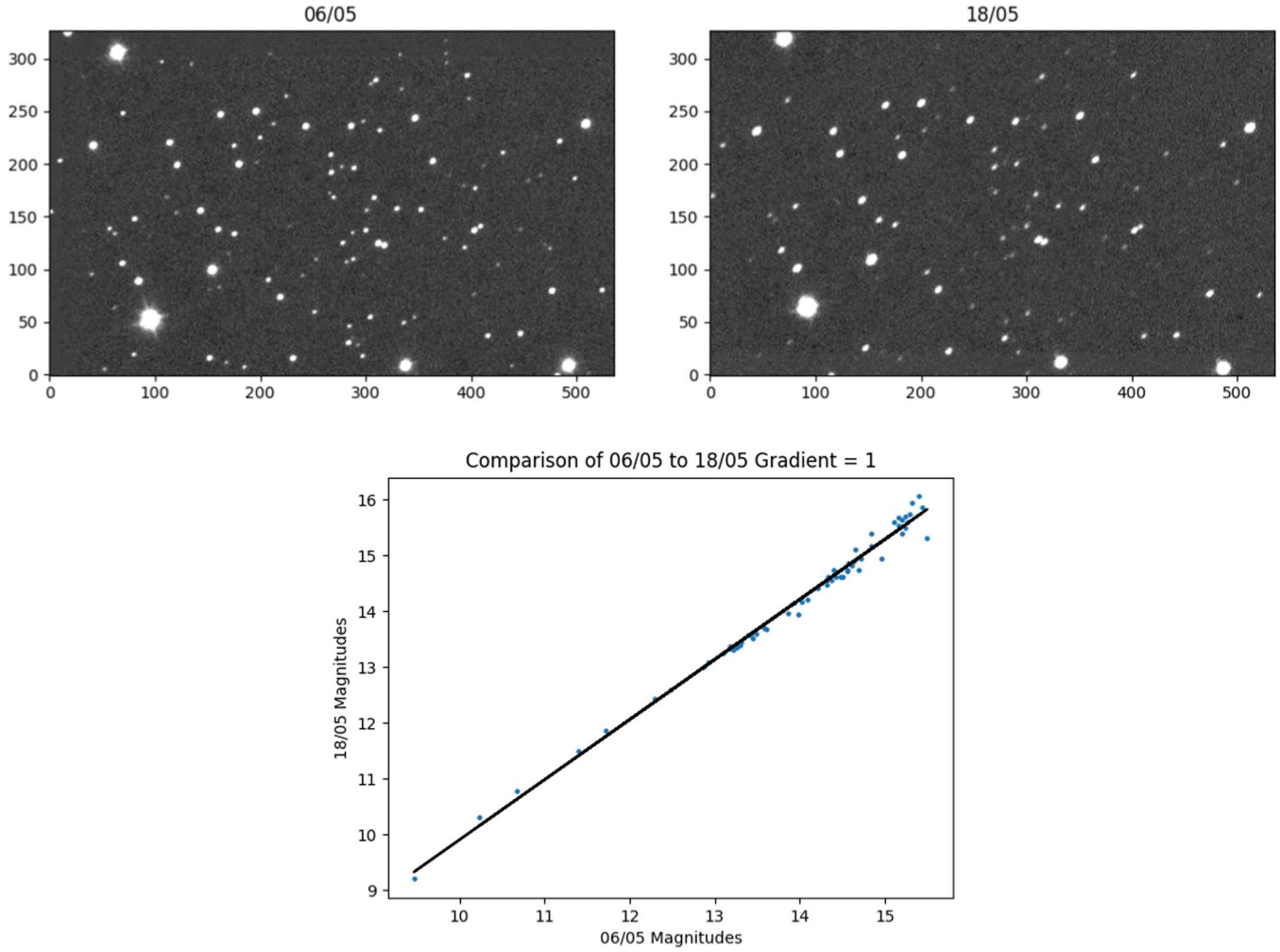

Figure 15. Comparison of NGC 2420 taken on two different nights. Top are the reduced images cropped to the same field of view, below is a comparison of stars shared between the images.

achieve a larger exposure time has equivalent results regarding the SNR of measurements. The data shows an SNR >1000 for sources brighter than $H = 10$ giving milli-magnitude precision for this range. For the three minute total exposure, 16 mag targets were achieved with an SNR of 10 matching expectations from theoretical sensitivity.

5. Conclusion

Testing has concluded on the instrument to assess its capabilities for astronomical imaging on the Liverpool Telescope with a summary of values shown in Table 4. Our results confirm that the Ninox 640 camera is suited to meet the science goals of the instrument, and the fore optics design has had the desired effect in reducing plate scale to meet requirements for Nyquist sampling at the La Palma site.

The instrument's linearity is excellent within the count region where readout noise and bit-depth saturation effects are not dominant, and is shown to be within a few tenths of a per cent. The conversion gain and readout noise have been calculated to show 0.52 e^- ADU^{-1} and 32 e^- respectively, with a good agreement to the PTC. The instrument's images' primary noise source is the FPN, which causes an rms of 33% signal level at 20% pixel saturation levels. This FPN consists of photoresponse non-uniformity, removed via flat-field correction, and dark signal non-uniformity, removed through image subtraction.

The dark current strongly depends on system temperature due to the small band-gap of the InGaAs alloy. At the operating temperature of -20°C, the dark current has a mean level of 1579 ADU s^{-1}, which, with read noise and bias level, will saturate the pixels at $\sim$10 s. However, this will not impact observations as IR sky brightness exceeds this count level, and therefore, images from the instrument are sky-limited and constructed through co-adding shorter exposures. Many

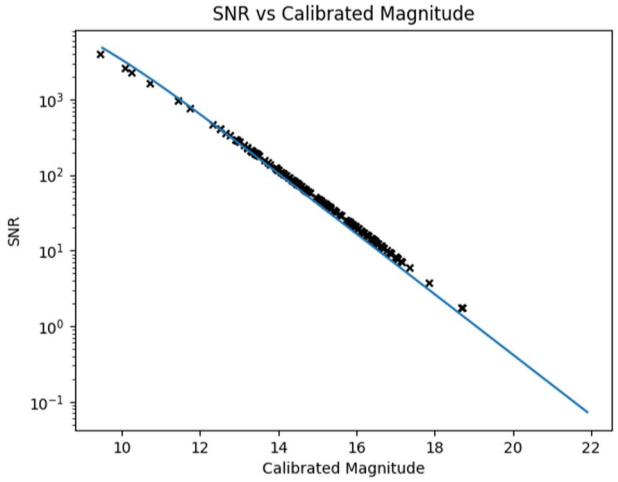

Figure 16. SNR values for NGC 2420 with a total exposure time of 180 s. On-sky data values are displayed as black crosses with the blue line representing theoretical SNR calculated in the same manner as Figure 3 with updated values for the nights sky-brightness and zero-point.

Table 4
Summary Table of Recorded Performance Figures

Parameter	Value
Dark Current	821^{+28}_{-21} $e^- s^{-1} pix^{-1}$
Gain	$0.52^{+0.18}_{-0.05}$ $e^- ADU^{-1}$
Read noise	32^{+9}_{-1} $e^- pix^{-1}$
bit-depth	8520^{+2949}_{-891} e^-
Average zero-point	22.8
Pixel scale	$0\farcs302$ pix^{-1}
H'-band wavelength range	1450–1700 nm

Note. All values were found with the detector at the operating temperature of −20°C.

vendors, including Raptor Photonics Ltd, now produce newer CMOS, SWIR cameras with improved sensors and cooling systems, drastically lowering the dark current. This reduction in dark current may improve sensitivity for passbands of lower wavelength (with fainter sky background levels), allowing the use of more of the InGaAs detector's spectral response in astronomy.

On-sky testing with the instrument has shown excellent results in meeting its sensitivity requirements and consistency over observations. On-sky sensitivity has matched the theory and is capable of 16th magnitude targets with SNR ∼ 10 for 180 s exposure time. This sensitivity makes it an appropriate instrument for follow up of targets found in surveys like Palomar Grattini IR and for initial follow-up of GW170817 like events.

Testing also produced an optimal observation technique to acquire flats, darks and calibration images using a dithering technique. Following the characterization of the camera, we plan to develop the instrument further. First, the instrument will include a custom moving stage to perform the dithering automatically during observations rather than by (slow) telescope pointing offsets. Although plans for the instrument also include developing a filter wheel with *Y*, *J* and *H*-band filters to make use of the whole maximum QE region, the sky-limited performance presented in this paper is solely for *H*-band measurements and does not extend to *Y* or *J* where the sky is somewhat fainter.

The Liverpool Telescope is operated on the island of La Palma by Liverpool John Moores University in the Spanish Observatorio del Roque de los Muchachos of the Instituto de Astrofisica de Canarias with financial support from the UK Science and Technology Facilities Council.

This publication makes use of data products from the Two Micron All Sky Survey, which is a joint project of the University of Massachusetts and the Infrared Processing and Analysis Center/California Institute of Technology, funded by the National Aeronautics and Space Administration and the National Science Foundation.

K.A.B. acknowledges support from an STFC, jointly supported by the Faculty of Engineering and Technology at LJMU.

We would like to thank Raptor Photonics Ltd. for useful discussions.

And finally, We thank the anonymous referee for their comments which led to a number of improvements to this paper.

ORCID iDs

Kristoffor Batty https://orcid.org/0000-0003-2088-6657

References

Abbott, B. P., Abbott, R., Abbott, T., et al. 2017, PhRvL, 119, 161101
Abbott, B. P., Abbott, R., Abbott, T. D., et al. 2016, ApJL, 832, L21
Bellm, E. 2014, in The Third Hot-wiring the Transient Universe Workshop, Vol. 27 (Santa Fe, NM)
Benn, C. R., & Ellison, S. L. 1998, New Astron. Rev., 42, 503
Copperwheat, C., Steele, I. A., Piascik, A., et al. 2016, MNRAS, 462, 3528
Hsieh, C. C., Wu, C. Y., Jih, F. W., & Sun, T. P. 1997, IEEE Transactions on Circuits and Systems for Video Technology, 7, 594
Kasliwal, M. M., Bally, J., Masci, F., et al. 2017, ApJ, 839, 88
Leyris, C., Martinez, F., Valenza, M., et al. 2006, in 2006 Proc. 32nd European Solid-State Circuits Conf. (Montreaux: IEEE), 376
Lourie, N. P., Baker, J. W., Burruss, R. S., et al. 2020, Proc. SPIE, 11447, 114479K
Magnier, E. A., Sweeney, W., Chambers, K., et al. 2020, ApJS, 251, 5

Moore, A. M., Kasliwal, M. K., Gelino, C. R., et al. 2016, Proc. SPIE, 9906, 99062C
Pian, E., D'Avanzo, P., Benetti, S., et al. 2017, Natur., 551, 67
Simcoe, R. A., Fűrész, G., Sullivan, P. W., et al. 2019, AJ, 157, 46
Skrutskie, M., Cutri, R., Stiening, R., et al. 2006, AJ, 131, 1163
Smartt, S., Chen, T. W., Jerkstrand, A., et al. 2017, Natur., 551, 75
Soon, J., Adams, D., De, K., et al. 2020, Proc. SPIE, 11203, 1120307
Steele, I. A., Smith, R. J., Rees, P. C., et al. 2004, Proc. SPIE, 5489, 679
Strausbaugh, R., Jackson, R., & Butler, N. 2018, PASP, 130, 095001
Tanvir, N. R., Levan, A., González-Fernández, C., et al. 2017, ApJL, 848, L27
Tonry, J., Denneau, L., Heinze, A., et al. 2018, PASP, 130, 064505
Wang, F., & Theuwissen, A. 2017, Electronic Imaging, 2017, 84